Journal of Solid State Chemistry 211 (2014) 106–112

Contents lists available at ScienceDirect

Journal of Solid State Chemistry

journal homepage: www.elsevier.com/locate/jssc

Optical and transport properties of $LaTi_{1-x}M_x(O,N)_{3\pm\delta}$ ($x=0$; 0.1, $M=Nb^{5+}$, W^{6+}) thin films prepared by plasma ammonolysis

Alexandra E. Maegli, Leyre Sagarna, Sascha Populoh, Bartosz Penkala, Eugenio H. Otal, Anke Weidenkaff*

Empa—Swiss Federal Laboratories for Materials Science and Technology, Solid State Chemistry and Catalysis, Ueberlandstr. 129, CH-8600 Duebendorf, Switzerland

ARTICLE INFO

Article history:
Received 24 October 2013
Received in revised form
6 December 2013
Accepted 9 December 2013
Available online 16 December 2013

Keywords:
Thin films
Microwave-induced plasma ammonolysis
X-ray photoelectron spectroscopy
UV–Vis transmittance
Electronic properties

ABSTRACT

Oxynitride thin films of composition $LaTi_{1-x}M_x(O,N)_{3\pm\delta}$ with $x=0$; 0.1 and $M=Nb^{5+}$, W^{6+} were prepared by nitridation *via* microwave-induced plasma (MIP) ammonolysis, which allowed keeping the nitridation time short (16 min). The higher possible oxidation states of the *B*-site substituents (Nb^{5+}, W^{6+}) with respect to Ti^{4+} caused higher N content for $LaTi_{0.9}Nb_{0.1}(O,N)_{3\pm\delta}$ and $LaTi_{0.9}W_{0.1}(O,N)_{3\pm\delta}$ compared to $LaTiO_2N$ due to charge-compensation. XPS O 1*s* and N 1*s* core level and valence band spectra evidenced for increasing N content in the order $LaTiO_2N < LaTi_{0.9}Nb_{0.1}(O,N)_{3\pm\delta} < LaTi_{0.9}W_{0.1}(O,N)_{3\pm\delta}$. All films were N deficient comparing with their stoichiometric formulas and assuming cations in highest oxidation states. Along with increasing N content, the bandgaps decreased from 2.4 to 2.2 and 2.1 eV for $LaTiO_2N$, $LaTi_{0.9}Nb_{0.1}(O,N)_{3\pm\delta}$, and $LaTi_{0.9}W_{0.1}(O,N)_{3\pm\delta}$ and the electronic conductivities increased along with the decreased bandgaps. The Seebeck coefficients at 860 K indicated the highest charge-carrier density for $LaTi_{0.9}W_{0.1}(O,N)_{3\pm\delta}$.

1. Introduction

Oxynitrides have received much attention due to their optical properties offering a broad field of applications such as ecologically friendly pigments [1–3], phosphors [4,5], solar selective coatings (high absorbance in the visible spectral range and low thermal emittance in the infrared region) [6,7], photocatalysts, and electrodes in photoelectrochemical water splitting cells [8–11]. The electronic structure is closely related to the chemical composition (*i.e.* the O/N ratio) as the less electronegative N 2*p* orbitals are located energetically above the O 2*p* orbitals. This results in a diminished bandgap width and shifts the absorption-edge energy into to the range of visible light [12]. Cationic co-substitution allows adjusting the N content due to charge-compensation mechanisms; therefore is the bandgaps width tuneable [13–15]. Thin films are required for many application of oxynitrides *e.g.* as photoelectrodes and coatings. Oxynitride thin films are mainly prepared by one of the following three routes. The first method involves the deposition of an oxide film, *e.g.* by pulsed laser deposition or spin-coating, with subsequent thermal ammonolysis [16,17]. A second route is a one-step deposition process by radio-frequency magnetron sputtering of an oxynitride target [11,18,19], or by pulsed reactive crossed beam laser ablation of an oxide target [20–22]. A third method, frequently used for the fabrication of photoelectrodes, is the deposition of oxynitride particles on a conductive substrate by electrophoretic deposition [23]. Photoelectrodes prepared by the latter method require post-treatments for sufficient particle–particle and particle–substrate connectivity to ensure charge-carrier transport [24,25]. Transport properties of oxide films are often improved by substitutional doping with higher-valent cations that increase the carrier concentration [26,27]. Electron doping for oxynitride materials is non-trivial because the additional cationic charges can be compensated by an increased N content; *i.e.* when La^{3+} replaces Sr^{2+} in $SrTiO_3$ to yield $LaTiO_3$, Ti(IV) is reduced to Ti(III), however, for the oxynitride $LaTiO_2N$, the oxidation state remains Ti(IV) [14]. Nonetheless, cationic co-substitution in oxynitrides is highly interesting as it allows modifying the bandgap and therefore the conductivity. The synthesis of oxynitride films for technical applications should be simple, cheap, and facile to produce substituted materials. Nitridation by microwave-induced plasma (MIP) ammonolysis has been much less investigated than thermal ammonolysis in spite of its advantages such as being widely applicable and having increased reactivity compared to thermal ammonolysis [28,29]. Therefore, shortened reaction times with a minimized NH_3 consumption are feasible by MIP ammonolysis [30,31].

In this context, we report on a novel synthesis route for oxynitride thin films of the composition $LaTi_{1-x}M_x(O,N)_{3\pm\delta}$ with

* Corresponding author. Tel.: +41 58 765 4212.
E-mail address: Anke.Weidenkaff@empa.ch (A. Weidenkaff).

0022-4596/$ - see front matter © 2013 Elsevier Inc. All rights reserved.
http://dx.doi.org/10.1016/j.jssc.2013.12.008

$x=0$; 0.1 and $M=Nb^{5+}$, W^{6+}. A precursor solution was spin-coated on Al_2O_3 substrates followed by calcination and MIP ammonolysis (16 min). The effects of *B*-site substitution on the N uptake, the bandgap, the conductivity, and the Seebeck coefficient were studied.

2. Experimental

2.1. Materials

Perovskite-type oxynitride films of composition $LaTi_{1-x}M_x(O,N)_{3\pm\delta}$ with $x=0$; 0.1 and $M=Nb^{5+}$, W^{6+} were prepared in a two-step synthesis involving the fabrication of oxide films and the subsequent nitridation with a microwave-induced NH_3 plasma. The precursor solutions for the oxides were prepared *via* soft-chemistry synthesis based on a previously reported method [32,33]. $La(NO_3)_3\cdot 6H_2O$ (Merck, >99%) was dissolved in glacial acetic acid ($C_2H_4O_2$, Sigma-Aldrich, ≥99%) at 90 °C in the molar ratio 1/20. The mixture was further heated at 110 °C for 1 h to evaporate H_2O coming from $La(NO_3)_3\cdot 6H_2O$. The solution was cooled to room temperature. Acetylacetone ($C_5H_8O_2$, Merck, ≥99%) was added in the molar ratio of 1/20 (La/acetylacetone). A second solution was prepared where stoichiometric amounts of titanium isopropoxide ($Ti\{OCH(CH_3)_2\}_4$, Sigma-Aldrich, ≥97%) were mixed with acetylacetone according to a molar ratio of 1/20 (Ti/acetylacetone). For the *B*-site substituted samples, stoichiometric amounts of $NbCl_5$ (Sigma-Aldrich, ≥99%) and WCl_6 (Sigma-Aldrich, ≥99%) were dissolved in the latter mixture. Then, both complexed solutions were combined and ethylene glycol ($C_2H_6O_2$, Merck, ≥99%) was added in a 1/1 molar ratio of La/ethylene glycol.

Round, single crystalline, non-oriented sapphire substrates (Stettler Sapphire AG, 1 mm thickness, 20 mm diameter) were thoroughly cleaned with Deutracon liquid soap, distilled water, and acetone. The solution was deposited using a spin-coater (Primus STT 15) with 3500 rpm for 30 s. Next, the films were calcined with a heating ramp of 2.5 °C min^{-1} to 600 °C and with a heating ramp of 1 °C min^{-1} from 600 to 900 °C (holding time of 2 h). Five layers were deposited to ensure a reasonable thickness and the films were calcined after every layer. For the nitridation reaction, the oxide films were treated in a microwave induced NH_3 plasma (MIP ammonolysis) [28,30]. In detail, a domestic microwave oven Daewoo 2M218H MFI 2.45 GHz was equipped with a waveguide made of brass for increased radiation focus and homogeneity of the plasma. The gas was supplied via a small quartz glass tube (8 mm diameter) inserted into the cavity reactor (quartz glass, 32 mm diameter, 350 mm length) and the films were placed with a distance of 1.5 cm to the gas outlet. The NH_3 flow was set to 250 mL min^{-1} controlled with a Brooks 5850E flow controller and the reactor was continuously pumped by a rotary pump (Alcatel 2004A). After evacuation, the system was flushed with NH_3 for 5 min prior to the experiment and the reaction time was 16 min.

2.2. Characterization

A PANalytical X'Pert PRO MPD Θ-2Θ X-ray diffractometer equipped with a PIXcel detector operating in grazing angle mode (GIXRD) was used for phase identification. The incidence angle Ω was set to 1° and the films were measured with a step size of 0.05° from 20° to 80° (2Θ).

X-ray photoelectron spectra (XPS) were collected with a Physical Electronics (PHI) Quantum 2000 with a monochromatic X-ray source Al*K*α (1486.6 eV). The detail core level and valence band spectra were obtained with a pass energy set to 46.95 eV and a step width of 0.2 eV. The software CasaXPS was used for curve fitting and quantification. The spectra were referenced to the C 1*s* peak of adventitious carbon from ambient air contaminations at 284.8 eV to compensate for internal charging effects. The O/N ratios were obtained from the integrated areas of the respective peaks after Ar^+-sputtering (1 kV). The peak area of the lattice oxygen was obtained by subtracting the contribution of absorbed OH groups to the O 1*s* signal from the total area of the O 1*s* signal by deconvolution into two contributions. Relative sensitivity factors were used as provided by the PHI MultiPak library (N 1*s*: 0.499, O 1*s*: 0.733).

Transmittance and reflectance spectra were collected with a UV-3600 Shimadzu UV–VIS–NIR spectrophotometer from 200 to 900 nm. The absorption coefficient α was calculated from $\alpha=\ln((1-R)^2/T)/d$, where R is the reflectance, T is transmittance, and d is the film thickness. The Tauc relationship assuming a direct transition of $(\alpha h\nu)^2=(h\nu-E_g)$ allowed to determine the bandgap E_g [34].

The morphology and thickness of the films were studied by scanning electron microscopy (SEM) with a XL30 ESEM (FEI) operating at a voltage of 15 kV. The samples were cut with a diamond saw and placed on aluminium holders in horizontal orientation for top-view imaging and in perpendicular orientation for cross-section imaging. They were coated with carbon in order to ensure the conductivity of the electrons coming from the beam. A secondary electron (SE) detector was employed to characterize the top-view morphology of the films and a backscattered electron detector (BSD) gave the necessary contrast to measure the thickness of the films in the cross-section view.

Transport properties were determined employing the four-point method using a RZ2001i-h apparatus (Ozawa Science Co., Ltd., Nagoya, Japan) under an Ar flow of 50 mL min^{-1}.

3. Results and discussion

Polycrystalline oxide films of composition $LaTi_{1-x}M_xO_{3\pm\delta}$ with $x=0$; 0.1 and $M=Nb^{5+}$, W^{6+} were obtained after spin-coating and calcining five layers of the precursor solution on the sapphire substrates. Fig. 1(a)–(c) shows the XRD patterns measured in grazing-incidence mode (GIXRD) where all reflections could be indexed according to the $La_2Ti_2O_7$ phase (JCPDS 028-0517). No Nb or W segregations were observed. Fig. 1(a′)–(c′) illustrates the conversion of the oxide films into their corresponding oxynitrides with

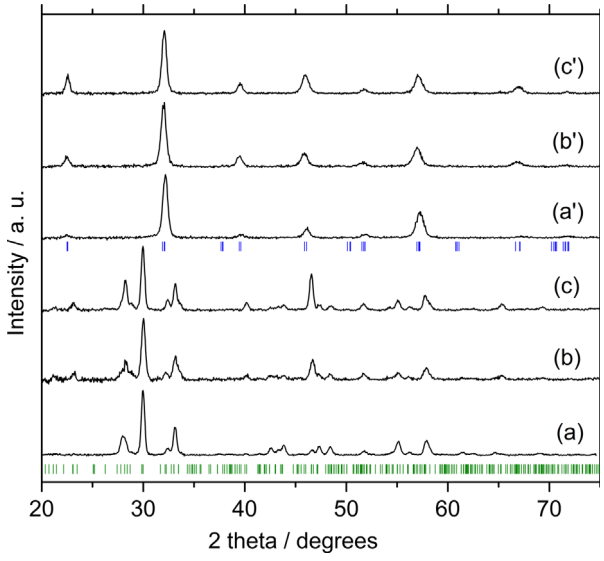

Fig. 1. GIXRD patterns of the oxide films (a) $La_2Ti_2O_7$, (b) $La_2Ti_{1.8}Nb_{0.2}O_{7.1}$, and (c) $La_2Ti_{1.8}W_{0.2}O_{7.2}$, and of the oxynitride films (a′) $LaTiO_2N$, (b′) $LaTi_{0.9}Nb_{0.1}(O,N)_{3\pm\delta}$, and (c′) $LaTi_{0.9}W_{0.1}(O,N)_{3\pm\delta}$. The green and blue vertical bars mark the reflections of $La_2Ti_2O_7$ and $LaTiO_2N$, respectively, given by the corresponding JCPDS PDF number. (For interpretation of the references to color in this figure legend, the reader is referred to the web version of this article.)

composition $LaTi_{1-x}M_x(O,N)_{3\pm\delta}$ (JCPDS 048-1230 for $LaTiO_2N$) after 16 min microwave induced plasma (MIP) ammonolysis.

SEM images after spin-coating and calcination in air illustrate a continuous coverage of the substrates with the respective films (Fig. 2). In $La_2Ti_2O_7$, needle-like structures were observed with an average length of 200 nm. $La_2Ti_{1.8}Nb_{0.2}O_{7.1}$ had a mosaic structure with domains of oriented needles of about 50 nm in length. The decomposition of the organics upon calcination leads to gaseous species that eventually evoked the bulges on the surface of $La_2Ti_{1.8}W_{0.2}O_{7.2}$ [35]. A fractured morphology of the films after plasma ammonolysis was observed. When the layered perovskite-type oxide phase ($A_2B_2X_7$) is converted into the simple perovskite-type oxynitride phase (ABX_3), lattice contraction due to the exchange of 3 O^{2-} with 2 N^{3-} occurs [36]. This has been observed to evoke a porous morphology in powdered samples [37,38]. Similarly, it can be assumed that lattice contraction induced the cracks in the thin films. Furthermore, the tension created at the interface upon different thermal expansion of the substrate and film was likely released by the formation of cracks.

The thickness of the three oxynitride films obtained by cross-sectional views are given in Table 1 and range from 0.25 μm for $LaTiO_2N$ to 0.86 μm for $LaTi_{0.9}Nb_{0.1}(O,N)_{3\pm\delta}$.

The transmittance spectra in Fig. 3 demonstrate red-shifted absorption edges of the substituted oxide films compared to $La_2Ti_2O_7$. The oscillating transmittance implied uniform thickness of the individual coatings while the different frequency and amplitude of the oscillations between the three films were caused by variations of their thicknesses and refractive indices [39]. The bandgaps of the oxide films, given in Table 1, were determined from Tauc plots (Fig. S1) and they ranged from 4.0 to 3.6 eV for $La_2Ti_2O_7$ and $La_2Ti_{1.8}W_{0.2}O_{7.2}$, respectively.

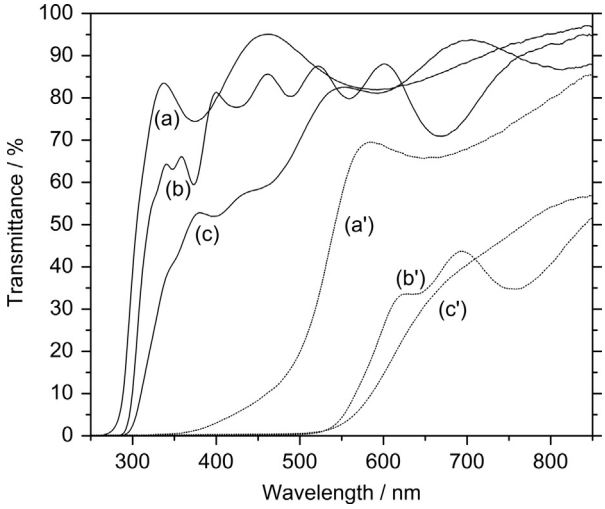

Fig. 3. Transmittance spectra of the oxides (a) $La_2Ti_2O_7$, (b) $La_2Ti_{1.8}Nb_{0.2}O_{7.1}$, and (c) $La_2Ti_{1.8}W_{0.2}O_{7.2}$, and the oxynitrides (a′) $LaTiO_2N$, (b′) $LaTi_{0.9}Nb_{0.1}(O,N)_{3\pm\delta}$, and (c′) $LaTi_{0.9}W_{0.1}(O,N)_{3\pm\delta}$.

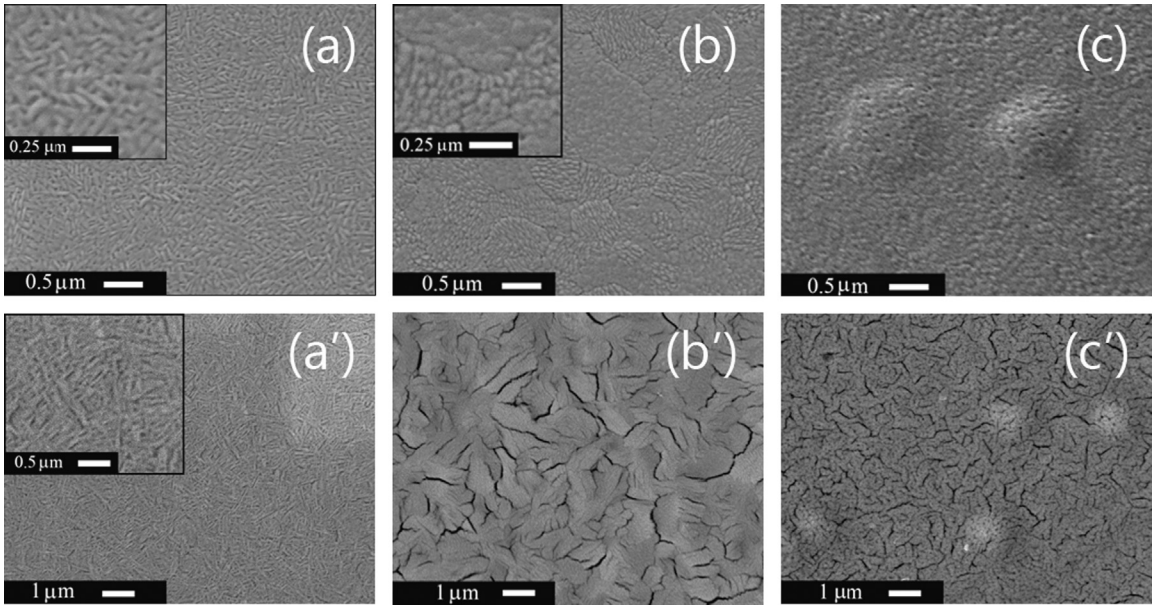

Fig. 2. SEM images of the oxide films (a) $La_2Ti_2O_7$, (b) $La_2Ti_{1.8}Nb_{0.2}O_{7.1}$, and (c) $La_2Ti_{1.8}W_{0.2}O_{7.2}$, and of the oxynitride films (a′) $LaTiO_2N$, (b′) $LaTi_{0.9}Nb_{0.1}(O,N)_{3\pm\delta}$, and (c′) $LaTi_{0.9}W_{0.1}(O,N)_{3\pm\delta}$.

Table 1
Summary of physical and chemical properties of oxynitride $LaTi_{1-x}M_x(O,N)_{3\pm\delta}$ films and the bandgap values of oxide $LaTi_{1-x}M_xO_{3\pm\delta}$ films.

Sample[a]	Thickness[b](μm)	Electronegativity (χ)	N/(O+N)[c]	Ti $2p_{3/2}$ peak area ratio of O–Ti–N/Ti–O[c]	Bandgap (eV)	Seebeck coefficient at 860 K (μV K^{-1})
LTON	0.250	Ti (1.5) O (3.4) N (3.0)	0.18	1.18	2.4 (Oxide: 4.0)	n. d.
LT(Nb)ON	0.860	Nb (1.6)	0.25	1.29	2.2 (Oxide: 4.0)	−591.52
LT(W)ON	0.600	W (1.7)	0.27	1.99	2.1 (Oxide: 3.6)	−413.00

[a] LTON, LT(Nb)ON, and LT(W)ON refer to $LaTiO_2N$, $LaTi_{0.9}Nb_{0.1}(O,N)_{3\pm\delta}$, and $LaTi_{0.9}W_{0.1}(O,N)_{3\pm\delta}$, respectively.
[b] Determined from SEM cross-sections.
[c] Quantified by XPS.

Fig. 4(A) shows the valence band spectra that are formed by O 2*p* orbitals, measured by XPS. No significant electronic changes of the valence band maximum (VBM) were caused by the *B*-site substitution in the oxide films; hence, the observed differences of the bandgap values must have been due to changes related to the conduction band. The conduction band minimum (CBM) is formed by antibonding π^*-combinations of transition-metal dt_{2g} and O 2*p* orbitals [40]. The dt_{2g} orbitals of more electronegative transition-metal ions are energetically closer located to the anionic 2*p* orbitals explaining the smaller values obtained for the *B*-site substituted oxides compared to $La_2Ti_2O_7$ [2].

The transparent oxide films were transformed into orange–brown translucent oxynitride films. Accordingly, the transmittance spectra shows red-shifted absorption edges of the oxynitride films (Fig. 3). The absorption edges of the oxynitrides were less steep compared to the oxides. This phenomenon has been reported for other oxynitrides and was attributed to a lower homogeneity of the Ti environment due to O/N disorder [14]. As N diffusion was progressing from the film surface toward the bulk, a gradient in the O/N ratio seemed likely, changing the surrounding of individual Ti ions and causing a spread of the absorption edge. The N/(O+N) ratios obtained by XPS analysis given in Table 1 evidenced N deficiency for all samples compared to the ideal stoichiometry ($LaTiO_2N$ with N/(O+N)=0.33). Incomplete transformation into the oxynitride in XRD phase-pure $LaTiO_2N$ is a frequently observed phenomenon in films and powders [11,18,20]. As reported, the presence of oxygen-rich intermediate-phases on atomic scale and without periodic ordering is possible; therefore, such intermediate phases are not detectable by means of XRD [41]. The N/(O+N) ratios were increasing for Nb- and W-substituted films, *i.e.* from 0.18 to 0.25 and 0.27 for $LaTiO_2N$, $LaTi_{0.9}Nb_{0.1}(O,N)_{3\pm\delta}$, and $LaTi_{0.9}W_{0.1}(O,N)_{3\pm\delta}$, respectively. This trend was reflected in the bandgap values which decreased from 2.4 to 2.2 and 2.1 eV for $LaTiO_2N$, $LaTi_{0.9}Nb_{0.1}(O,N)_{3\pm\delta}$, and $LaTi_{0.9}W_{0.1}(O,N)_{3\pm\delta}$, respectively. Due to N defects, the bandgap of $LaTiO_2N$ (2.4 eV) was about 0.2 eV larger than the reported values for stoichiometric $LaTiO_2N$ [11,15,42]. The XPS valence band spectra in Fig. 4(B) evidenced that the electronic density near the Fermi level was increased due to the mixing of N 2*p* and O 2*p* orbitals. The different N contents were mirrored in the VBM positions that were shifted from 0.8 ($LaTiO_2N$) to 0.6 ($LaTi_{0.9}Nb_{0.1}(O,N)_{3\pm\delta}$) and 0.5 eV ($LaTi_{0.9}W_{0.1}(O,N)_{3\pm\delta}$). Not only the N content but also the averaged electronegativity-increase of the *B*-site elements in the substituted films relative to $LaTiO_2N$ diminished the bandgaps of the former.

XPS Ti 2*p* detail spectra of the oxide $La_2Ti_2O_7$ (Fig. 5(A)) recorded the Ti $2p_{3/2}$ peaks at 458.1 eV as was reported for Ti^{4+} in $La_2Ti_2O_7$ [43]. The Ti $2p_{3/2}$ peaks were shifted to higher binding energies for the *B*-site substituted oxides. It was related to an inductive effect of Nb (χ=1.6) and W (χ=1.7) being more electronegative than Ti (χ=1.5) and therefore decreasing the electron density on Ti. Along with the positive shift of the Ti $2p_{3/2}$ peak, its FWHM increased from 1.2 eV for $La_2Ti_2O_7$ to 1.6 eV for $LaTi_{0.9}W_{0.1}(O,N)_{3\pm\delta}$ because the chemical environment of Ti^{4+} ions changed depending on *B*-site substituents. For the oxynitrides, a new peak at lower binding energies of the Ti $2p_{3/2}$ spectra appeared (Fig. 5(B)). This new peak was not fully resolved for Ti $2p_{1/2}$ but only visible as a peak broadening due to the smaller intensity and larger FHWM compared with Ti $2p_{3/2}$. The position and shape of the Ti $2p_{3/2}$ peak in oxynitrides is under discussion in literature as some reports evidenced for a dual peak and others demonstrated the signature of a single broad peak [44,45]. Here, the peak was positioned at around 456.7 eV and indicated a different chemical environment or lowered oxidation state of Ti. The reported value for Ti^{3+} in TiN is with 455.3 eV clearly lower than observable here [46]. According to literature, the peak of Ti in O–Ti–N bonds is located at 456.5 eV which matches closely the values obtained here [47,48]. The signature of the O–Ti peak was still present and therefore indicates that a part of the Ti octahedra did not contain N. This finding corroborates the previously discussed N deficiency. The integrated area ratios between the two peaks related to O–Ti–N and to O–Ti are given in Table 1. The contribution of the O–Ti–N peak increased for $LaTi_{0.9}Nb_{0.1}(O,N)_{3\pm\delta}$ and even more for $LaTi_{0.9}W_{0.1}(O,N)_{3\pm\delta}$ compared to $LaTiO_2N$ confirming the increased N content of the former two (Table 1).

The oxidation states of Nb and W in the *B*-site substituted oxide films were assigned to W^{6+} and Nb^{5+} by comparing with reference spectra of Nb_2O_5 and WO_3, (Fig. 6(A) and (B)). In contrast to the simple perovskite-type structure where anionic excess is not possible due to the close-packed structure, the layered $La_2Ti_2O_7$ allows for O excess by increasing the density of O slabs between the TiO_6 octahedral blocks [49,50]. After MIP ammonolysis, Nb 3*p* as well as W 4*d* doublets of the oxynitrides

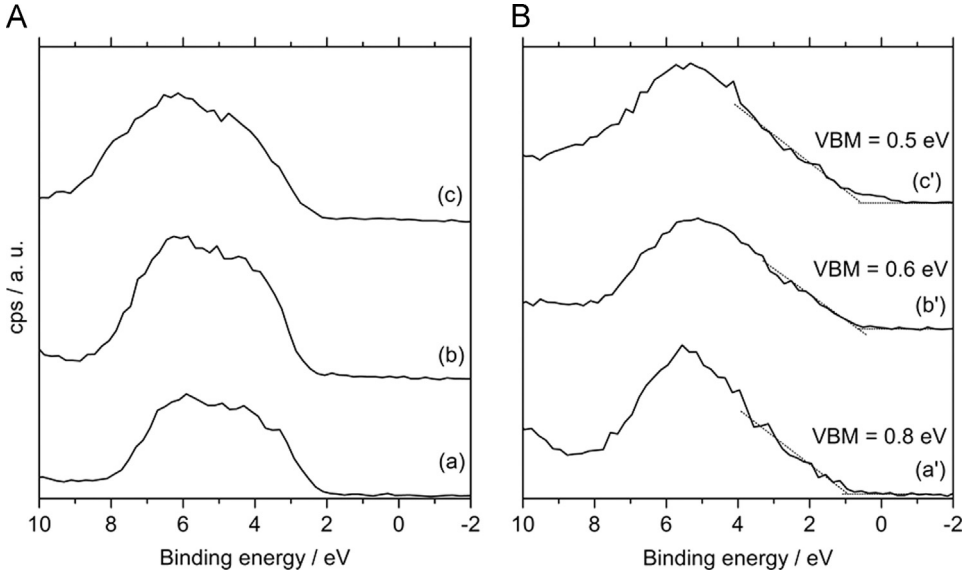

Fig. 4. XPS valence band spectra of (A) oxides (a) $La_2Ti_2O_7$, (b) $La_2Ti_{1.8}Nb_{0.2}O_{7.1}$, and (c) LT(W)O and of (B) oxynitrides (a′) $LaTiO_2N$, (b′) $LaTi_{0.9}Nb_{0.1}(O,N)_{3\pm\delta}$, and (c′) $LaTi_{0.9}W_{0.1}(O,N)_{3\pm\delta}$.

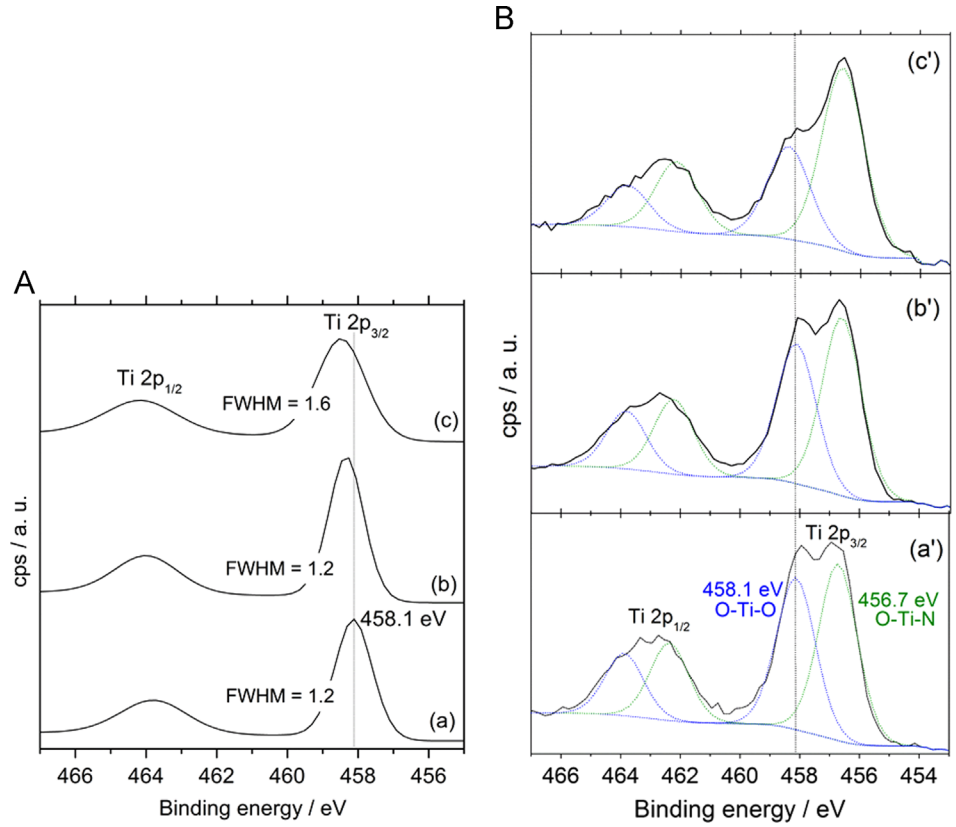

Fig. 5. (A) XPS Ti 2*p* spectra of the oxides (a) $La_2Ti_2O_7$, (b) $La_2Ti_{1.8}Nb_{0.2}O_{7.1}$, and (c) $La_2Ti_{1.8}W_{0.2}O_{7.2}$. (B) XPS Ti 2*p* spectra after MIP ammonolyis the oxynitrides (a′) $LaTiO_2N$, (b′) $LaTi_{0.9}Nb_{0.1}(O,N)_{3\pm\delta}$, and (c′) $LaTi_{0.9}W_{0.1}(O,N)_{3\pm\delta}$.

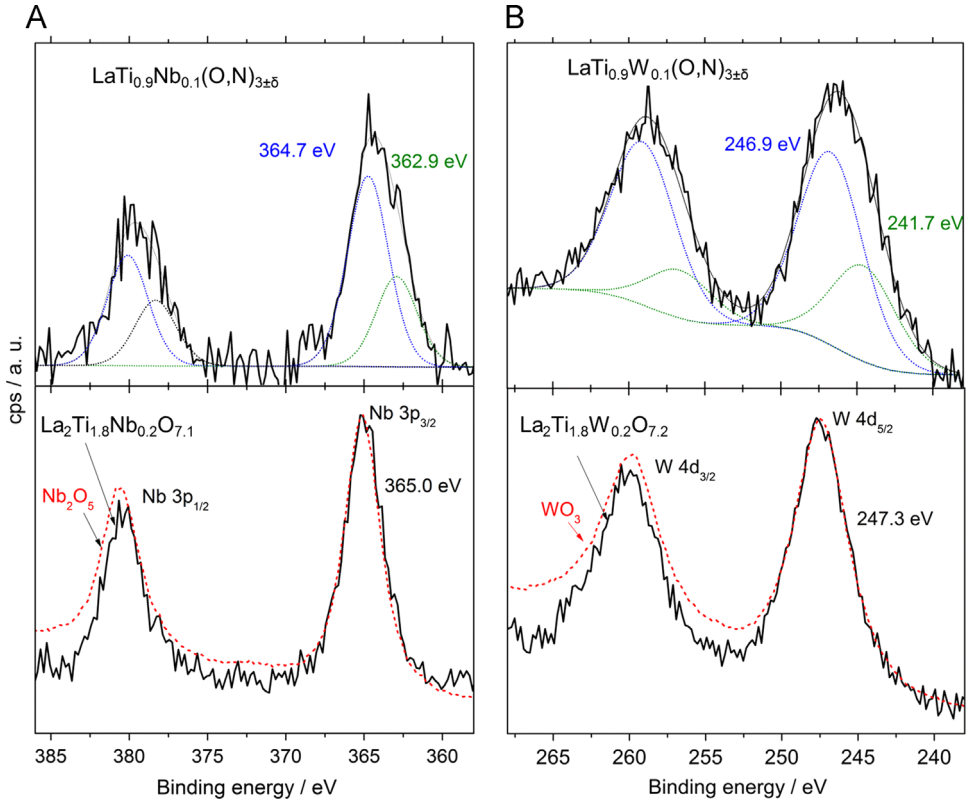

Fig. 6. (A) XPS Nb 3*p* spectra in $La_2Ti_{1.8}Nb_{0.2}O_{7.1}$ and reference Nb_2O_5 (bottom panel), and $LaTi_{0.9}Nb_{0.1}(O,N)_{3\pm\delta}$ (top panel). (B) XPS W 4*d* spectra in $La_2Ti_{1.8}W_{0.2}O_{7.2}$ and reference WO_3 (bottom panel) and $LaTi_{0.9}W_{0.1}(O,N)_{3\pm\delta}$ (top panel).

were broadened and asymmetric towards lower binding energies. Likewise to the Ti spectra, the reason was supposed to lie in the changed chemical environment for Nb (O–Nb–N) and W (O–W–N). Furthermore, a partial reduction of Nb^{5+} and W^{6+} to lower oxidation states could not be excluded because the more electronegative cations are often not stabilized in their highest oxidation state due to the reductive atmosphere during ammonolysis [51,52].

The films showed semiconducting behaviour with high resistivity at room temperature. Therefore, conductivity was only measurable at higher temperatures, *i.e.* above 600 K for $LaTi_{0.9}W_{0.1}(O,N)_{3\pm\delta}$ and 760 K for $LaTiO_2N$ and $LaTi_{0.9}Nb_{0.1}(O,N)_{3\pm\delta}$ (Fig. 7). The conductivity was highest for $LaTi_{0.9}W_{0.1}(O,N)_{3\pm\delta}$ followed by $LaTi_{0.9}Nb_{0.1}(O,N)_{3\pm\delta}$ and $LaTiO_2N$. The grain boundaries and the cracked morphology presumably degraded the mobility leading to poorly conducting films. In agreement to our results, $LaTiO_2N$ films prepared by PLD [16] and spin-coating [17] were reported to be insulating at room temperature. On the other hand, $LaTiO_2N$ films prepared by radio-frequency magnetron sputtering had a conductivity of 0.08 S cm^{-1} at room temperature [18]. Depending on the preparation procedure, the morphology of the films and also oxidation state of the transition-metal ions can be different and affect the electrical conductivity. In oxynitrides, the conductivity also might be deteriorated due to morphological peculiarities like pore-formation upon the oxide-oxynitride conversion [53]. The increasing conductivity ($LaTiO_2N < LaTi_{0.9}Nb_{0.1}(O,N)_{3\pm\delta} < LaTi_{0.9}W_{0.1}(O,N)_{3\pm\delta}$) can be associated with the decreasing width of the bandgap ($LaTiO_2N > LaTi_{0.9}Nb_{0.1}(O,N)_{3\pm\delta} > LaTi_{0.9}W_{0.1}(O,N)_{3\pm\delta}$). Electron doping by higher-valent cations increases the conductivity in metal oxides [54]. In oxynitrides, however, the additional positive charges of the substituents could have been compensated by increasing N content. On the other hand, the possibility of reduced Nb and W oxidation states was discussed in the XPS section. This would increase the density of conduction-band electrons for the *B*-site substituted samples relative to $LaTiO_2N$. It cannot be ruled out that different morphologies had an impact on the results. However, the trend of increasing charge carrier density in the order $LaTiO_2N < LaTi_{0.9}Nb_{0.1}(O,N)_{3\pm\delta} < LaTi_{0.9}W_{0.1}(O,N)_{3\pm\delta}$ as seen in the conductivity measurements was supported by the Seebeck coefficients (Table 1). The Seebeck coefficient is inversely proportional to the charge carrier density. They were measured to be $-591.52\ \mu V\ K^{-1}$ for $LaTi_{0.9}Nb_{0.1}(O,N)_{3\pm\delta}$ and $-413.00\ \mu V\ K^{-1}$ for $LaTi_{0.9}W_{0.1}(O,N)_{3\pm\delta}$ at 860 K while it was not possible to measure it for $LaTiO_2N$ due to its low electrical conductivity. The sign of the Seebeck coefficient was negative as expected for electrical conductivity dominated by electrons.

To assess the photoelectrochemical properties of the films, $LaTiO_2N$ and $LaTi_{0.9}Nb_{0.1}(O,N)_{3\pm\delta}$ were selected for the measurements, the latter due to its increased electronic conductivity. Photocurrents were observed for both compositions under visible light irradiation while a substantial dark current was present (Fig. S2). This observation suggests that MIP ammonolysis could offer a novel route to obtain $LaTiO_2N$ electrodes for PEC applications.

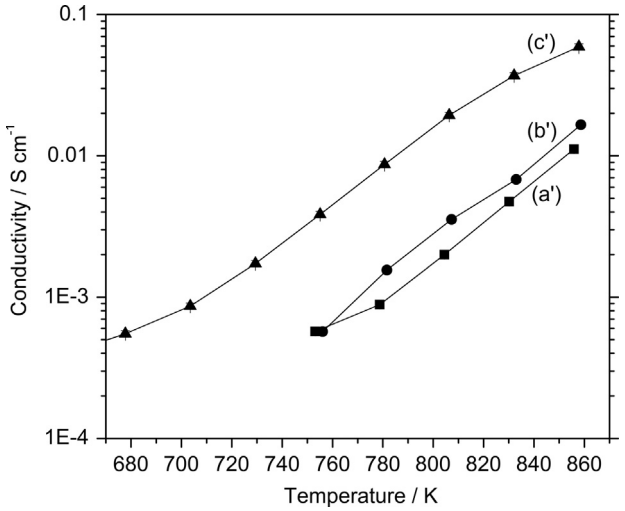

Fig. 7. Conductivity of (a′) $LaTiO_2N$, (b′) $LaTi_{0.9}Nb_{0.1}(O,N)_{3\pm\delta}$, and (c′) $LaTi_{0.9}W_{0.1}(O,N)_{3\pm\delta}$.

4. Conclusion

Polycrystalline and randomly oriented unsubstituted and *B*-site substituted $LaTi_{1-x}M_x(O,N)_{3\pm\delta}$ with $x=0$; 0.1 and $M=Nb^{5+}$, W^{6+} thin films were fabricated by spin coating an oxide precursor solution on sapphire substrates, calcination, and nitridation with a microwave-induced NH_3 plasma. Regardless of the N deficiency found in all films, *B*-site substitution allowed for more N uptake compared to unsubstituted $LaTiO_2N$ due to the higher possible oxidation state (W^{6+} and Nb^{5+} compared to Ti^{4+}). Hence, the bandgap was reduced for $LaTi_{0.9}W_{0.1}(O,N)_{3\pm\delta}$ (2.1 eV) and $LaTi_{0.9}Nb_{0.1}(O,N)_{3\pm\delta}$ (2.2 eV) relative to $LaTiO_2N$ (2.4 eV). Likewise, the valence band maxima were shifted from 0.8 to 0.6 and 0.5 eV for $LaTiO_2N$, $LaTi_{0.9}Nb_{0.1}(O,N)_{3\pm\delta}$, and $LaTi_{0.9}W_{0.1}(O,N)_{3\pm\delta}$, respectively. The conductivity increased in the order $LaTiO_2N < LaTi_{0.9}Nb_{0.1}(O,N)_{3\pm\delta} < LaTi_{0.9}W_{0.1}(O,N)_{3\pm\delta}$ along with a decreased width of the bandgap. The increased conductivity was confirmed by the lower Seebeck coefficient for $LaTi_{0.9}W_{0.1}(O,N)_{3\pm\delta}$ compared to $LaTi_{0.9}Nb_{0.1}(O,N)_{3\pm\delta}$. Photoelectrochemical measurements showed the possibility of this synthesis approach to obtain photoanodes for solar water splitting applications.

Acknowledgments

We appreciate helpful discussions with Dr. Simone Pokrant and Dr. Songhak Yoon, Dr. James Eilertsen and Mr. Benjamin Süess from the group of Solid State Chemistry and Catalysis, Empa, Switzerland. The authors sincerely acknowledge the support of Dr.Takashi Hisatomi from the Laboratory of Catalysis, The University of Tokyo, Japan.

Appendix A. Supporting information

Supplementary data associated with this article can be found in the online version at http://dx.doi.org/10.1016/j.jssc.2013.12.008.

References

[1] M. Jansen, H.P. Letschert, Nature 404 (2000) 980.
[2] R. Aguiar, D. Logvinovich, A. Weidenkaff, A. Rachel, A. Reller, S.G. Ebbinghaus, Dyes Pigm. 76 (2008) 70.
[3] E. Günther, M. Jansen, Mater. Res. Bull. 36 (2001) 1399.
[4] M. Zhang, J. Wang, Z. Zhang, Q. Zhang, Q. Su, Appl. Phys. B 93 (2008) 829.
[5] R. Mueller-Mach, G. Mueller, M.R. Krames, H.A. Höppe, F. Stadler, W. Schnick, T. Juestel, P. Schmidt, Phys. Status Solidi A 202 (2005) 1727.
[6] H.C. Barshilia, N. Selvakumar, K.S. Rajam, A. Biswas, Sol. Energy Mater. Sol. Cells 92 (2008) 1425.
[7] C. Nunes, V. Teixeira, M.L. Prates, N.P. Barradas, A.D. Sequeira, Thin Solid Films 442 (2003) 173.
[8] K. Maeda, Phys. Chem. Chem. Phys. 15 (2013) 10537.
[9] K. Maeda, K. Domen, J. Phys. Chem. Lett. 1 (2010) 2655.
[10] K. Maeda, K. Domen, J. Phys. Chem. C 111 (2007) 7851.
[11] C. Le Paven-Thivet, A. Ishikawa, A. Ziani, L. Le Gendre, M. Yoshida, J. Kubota, F. Tessier, K. Domen, J. Phys. Chem. C 113 (2009) 6156.
[12] R. Marchand, C.R. Acad. Sci., Ser. IIc: Chim 2 (1999) 669.

[13] P. Wu, J. Shi, Z. Zhou, W. Tang, L. Guo, Int. J. Hydrogen Energy 37 (2012) 13704.
[14] F. Cheviré, F. Tessier, R. Marchand, Eur. J. Inorg. Chem. 2006 (2006) 1223.
[15] D. Logvinovich, A. Börger, M. Döbeli, S.G. Ebbinghaus, A. Reller, A. Weidenkaff, Prog. Solid State Chem. 35 (2007) 281.
[16] R. Aguiar, D. Logvinovich, A. Weidenkaff, H. Karl, C.W. Schneider, A. Reller, S.G. Ebbinghaus, Mater. Res. Bull. 43 (2008) 1376.
[17] R. Aguiar, A. Weidenkaff, C.W. Schneider, A. Reller, S.G. Ebbinghaus, Prog. Solid State Chem. 35 (2007) 291.
[18] C. Le Paven-Thivet, L. Le Gendre, J. Le Castrec, F. Cheviré, F. Tessier, J. Pinel, Prog. Solid State Chem. 35 (2007) 299.
[19] Y. Lu, A. Ziani, C. Le Paven-Thivet, R. Benzerga, L. Le Gendre, D. Fasquelle, H. Kassem, F. Tessier, V. Vigneras, J.C. Carru, A. Sharaiha, Thin Solid Films 520 (2011) 778.
[20] I. Marozau, A. Shkabko, M. Döbeli, T. Lippert, M. Mallepell, C.W. Schneider, A. Weidenkaff, A. Wokaun, Acta Mater. 59 (2011) 7145.
[21] I. Marozau, M. Döbeli, T. Lippert, D. Logvinovich, M. Mallepell, A. Shkabko, A. Weidenkaff, A. Wokaun, Appl. Phys. A 89 (2007) 933.
[22] I.C. Lekshmi, A. Gayen, M.S. Hegde, Mater. Res. Bull. 40 (2005) 93.
[23] R. Abe, M. Higashi, K. Domen, J. Am. Chem. Soc 132 (2010) 11828.
[24] R. Abe, T. Takata, H. Sugihara, K. Domen, Chem. Lett. 34 (2005) 1162.
[25] N. Nishimura, B. Raphael, K. Maeda, L. Le Gendre, R. Abe, J. Kubota, K. Domen, Thin Solid Films 518 (2010) 5855.
[26] Z. Li, W. Luo, M. Zhang, J. Feng, Z. Zou, Energy Environ. Sci. 6 (2013) 347.
[27] F.F. Abdi, L. Han, A.H.M. Smets, M. Zeman, B. Dam, R. van de Krol, Nat. Commun. (2013) 4.
[28] A. Shkabko, M.H. Aguirre, I. Marozau, M. Doebeli, M. Mallepell, T. Lippert, A. Weidenkaff, Mater. Chem. Phys. 115 (2009) 86.
[29] D.J. Brooks, R.E. Douthwaite, Rev. Sci. Instrum 75 (2004) 5277.
[30] S.G. Ebbinghaus, H.-P. Abicht, R. Dronskowski, T. Müller, A. Reller, A. Weidenkaff, Prog. Solid State Chem. 37 (2009) 173.
[31] A. Shkabko, M.H. Aguirre, P. Hug, A. Weidenkaff, I. Marozau, T. Lippert, IOP Conf. Ser.: Mater. Sci. Eng. 8 (2010) 012035.
[32] D. Paik, A.V.P. Rao, S. Komarneni, J. Sol–Gel Sci. Technol 10 (1997) 213.
[33] D.S. Alfaruq, E.H. Otal, M.H. Aguirre, S. Populoh, A. Weidenkaff, J. Mater. Res 27 (2012) 985.
[34] S.-S. Kim, S.-Y. Choi, C.-G. Park, H.-W. Jin, Thin Solid Films 347 (1999) 155.
[35] S. Sakka (Ed.), Handbook of Sol–Gel Science and Technology: Processing, Characterization and Applications, Kluwer Academic Publishers, 2005.
[36] N.-Y. Park, Y.-I. Kim, J. Mater. Sci 47 (2012) 5333.
[37] T. Takata, D. Lu, K. Domen, Cryst. Growth Des. 11 (2010) 33.
[38] D. Logvinovich, L. Bocher, D. Sheptyakov, R. Figi, S.G. Ebbinghaus, R. Aguiar, M.H. Aguirre, A. Reller, A. Weidenkaff, Solid State Sci. 11 (2009) 1513.
[39] X.B. Lu, Z.G. Liu, J. Electron. Mater 30 (2001) 554.
[40] H.W. Eng, P.W. Barnes, B.M. Auer, P.M. Woodward, J. Solid State Chem 175 (2003) 94.
[41] R. Aguiar, A. Kalytta, A. Reller, A. Weidenkaff, S.G. Ebbinghaus, J. Mater. Chem 18 (2008) 4260.
[42] A. Kasahara, K. Nukumizu, G. Hitoki, T. Takata, J.N. Kondo, M. Hara, H. Kobayashi, K. Domen, J. Phys. Chem. A 106 (2002) 6750.
[43] V.V. Atuchin, T.A. Gavrilova, J.C. Grivel, V.G. Kesler, J. Phys. D: Appl. Phys 42 (2009) 035305.
[44] Y. Masuda, R. Mashima, M. Yamada, K. Ikeuchi, K.-i. Murai, G.I.N. Waterhouse, J.B. Metson, T. Moriga, J. Ceram. Soc. Jpn 117 (2009) 76.
[45] Y. Lu, C. Le Paven, H.V. Nguyen, R. Benzerga, L. Le Gendre, S. Rioual, F. Tessier, F. Cheviré, A. Sharaiha, C. Delaveaud, X. Castel, Cryst. Growth Des. 13 (2013) 4852.
[46] N.C. Saha, H.G. Tompkins, J. Appl. Phys 72 (1992) 3072.
[47] H. Chen, A. Nambu, Wen, J. Graciani, Zhong, J.C. Hanson, E. Fujita, J.A. Rodriguez, J. Phys. Chem. C 111 (2006) 1366.
[48] F. Meng, Z. Hong, J. Arndt, M. Li, M. Zhi, F. Yang, N. Wu, Nano Res 5 (2012) 213.
[49] D.J. Buttrey, P. Ganguly, J.M. Honig, C.N.R. Rao, R.R. Schartman, G.N. Subbanna, J. Solid State Chem 74 (1988) 233.
[50] J. Canales-Vázquez, S. Tao, M. Patrakeev, J.T.S. Irvine, W. Zhou, J. Frade, MRS Online Proc. Lib 801 (7) (2003) 1.
[51] I.D. Fawcett, K.V. Ramanujachary, M. Greenblatt, Mater. Res. Bull. 32 (1997) 1565.
[52] F. Tessier, R. Marchand, J. Solid State Chem 171 (2003) 143.
[53] L. Sagarna, A.E. Maegli, S. Yoon, S. Populoh, A. Shkabko, S. Pokrant, K.Z. Rushchanskii, M. Ležaić, A. Weidenkaff, J. Appl. Phys 114 (2013) 1.
[54] D.M. Smyth, Aliovalent doping in perovskite oxides, in: W. Wong-Ng, T. Holesinger, G. Riley, R. Guo (Eds.), Perovskite Oxides for Electronic, Energy Conversion, and Energy Efficiency Applications, vol. 104, The American Ceramic Society, Ohio, 2000.